

Article

Reversible Redox Activity in Multicomponent Metal-Organic Frameworks Constructed from Trinuclear Copper Pyrazolate Building Blocks

Binbin Tu, Qingqing Pang, Huoshu Xu, Xiaomin Li, Yulin Wang, Zhen Ma, Linhong Weng, and Qiaowei Li

J. Am. Chem. Soc., **Just Accepted Manuscript** • Publication Date (Web): 25 May 2017

Downloaded from <http://pubs.acs.org> on May 25, 2017

Just Accepted

“Just Accepted” manuscripts have been peer-reviewed and accepted for publication. They are posted online prior to technical editing, formatting for publication and author proofing. The American Chemical Society provides “Just Accepted” as a free service to the research community to expedite the dissemination of scientific material as soon as possible after acceptance. “Just Accepted” manuscripts appear in full in PDF format accompanied by an HTML abstract. “Just Accepted” manuscripts have been fully peer reviewed, but should not be considered the official version of record. They are accessible to all readers and citable by the Digital Object Identifier (DOI®). “Just Accepted” is an optional service offered to authors. Therefore, the “Just Accepted” Web site may not include all articles that will be published in the journal. After a manuscript is technically edited and formatted, it will be removed from the “Just Accepted” Web site and published as an ASAP article. Note that technical editing may introduce minor changes to the manuscript text and/or graphics which could affect content, and all legal disclaimers and ethical guidelines that apply to the journal pertain. ACS cannot be held responsible for errors or consequences arising from the use of information contained in these “Just Accepted” manuscripts.

Reversible Redox Activity in Multicomponent Metal–Organic Frameworks Constructed from Trinuclear Copper Pyrazolate Building Blocks

Binbin Tu,[†] Qingqing Pang,[†] Huoshu Xu,[†] Xiaomin Li,[†] Yulin Wang,[‡] Zhen Ma,[‡] Linhong Weng,[†] Qiaowei Li^{*†}

[†]Department of Chemistry, iChEM (Collaborative Innovation Center of Chemistry for Energy Materials), and Shanghai Key Laboratory of Molecular Catalysis and Innovative Materials, Fudan University, Shanghai 200433, P. R. China

[‡]Department of Environmental Science and Engineering, Fudan University, Shanghai 200433, P. R. China

ABSTRACT: Inorganic functionalization of metal–organic frameworks (MOFs), such as incorporating multiple inorganic building blocks with distinct metals into one structure and further modulating the metal charges, endows the porous materials with significant properties towards their applications in catalysis. In this report, by exploring the role of 4-pyrazolecarboxylic acid (H₂PyC) in the formation of trinuclear copper pyrazolate as a metalloligand *in situ*, four new MOFs with multiple components in order were constructed through one-pot synthesis. This metalloligand strategy provides multicomponent MOFs with new topologies (**tub** for FDM-4 and **tap** for FDM-5), and is also compatible with a second organic linker for cooperative construction of complex MOFs (1,4-benzenedicarboxylic acid for FDM-6 and 2,6-naphthalenedicarboxylic acid for FDM-7). The component multiplicity of these MOFs originates from the PyC's capability of separating Cu and Zn due to their differentiated binding affinities towards pyrazolate and carboxylate. These MOFs feature reversible and facile redox transformations between Cu^I₃(PyC)₃ and Cu^{II}₃(μ-OH)(PyC)₃(OH)₃ without altering the connecting geometries of the units, thus further contributing to the significant catalytic activities in the oxidation of CO and aromatic alcohols, and the decomposition of H₂O₂. This study on programing multiple inorganic components into one framework and modulating their electronic structures is an example of functionalizing the inorganic units of MOFs with a high degree of control.

INTRODUCTION

The reticular chemistry of metal–organic frameworks (MOFs)¹ have been greatly enriched by attaching specific functional groups to the organic linkers using pre-synthetic² or post-synthetic approach³, and recently the strategy of using more than one linker in one pot has provided MOFs with multiple organic components⁴ and multivariate MOFs (MTV-MOFs)⁵. Compared with the various organic functionalization of MOF structures, inorganic functionalization, such as incorporating more than one metal in the framework⁶ or regulating the electronic structures of specific inorganic building blocks (such as switching the metal charge)⁷ in a controlled manner, is less explored but has gained increasing recognition.

We sought to pursue multicomponent MOFs, in which (i) different metal ions are organized into distinct secondary building units (SBUs)⁸ through one-pot synthesis, and (ii) the metals from these SBUs present switchable redox states while reserving the SBU geometry. Recently, 4-pyrazolecarboxylic acid (H₂PyC) as an organic linker has drawn our great attention, because the pyrazole and carboxylic acid feature distinguishable coordination affinities towards different metal ions.^{6f} Therefore, in addition to the frequently observed entities from three pyrazoles and three

metals, such as Cu,⁹ this binding divergence creates a second SBU based on a different metal on the carboxylic acid side. Furthermore, the trinuclear entities with different metal valences, the [Cu^I₃(HPyC)₃] (**3a** in Figure 1, the number **3** indicates the connectivity of the SBU) and [Cu^{II}₃(μ-OH)(HPyC)₃]²⁺ (**3b** in Figure 1), carry exact the same SBU geometry in the resulting frameworks and thus guarantee the integrity of the structures during the oxidation and reduction. By employing this characteristic building block, open and multicomponent structures could be rationally programed and synthesized, in which further modulation of the metal valence and the consequent unusual catalytic activities in compartmentalized spaces are expected.

In this report, we successfully synthesized two multicomponent MOFs with unprecedented topologies, namely FDM-4 and FDM-5, by combining H₂PyC as the only organic ligand, various Zn-based SBUs, and the triangular copper pyrazolate complex *in situ* as the metalloligand^{6c,10} in one pot. This synthetic strategy was further exemplified in the construction of two new MOFs, FDM-6 and FDM-7, where two types of struts with distinct geometries—the triangular metalloligand and the linear organic linker—were consolidated in an ordered fashion. Driven by the coordination pairing between the two metal ions and the two ends of PyC, the self-organization of the various building

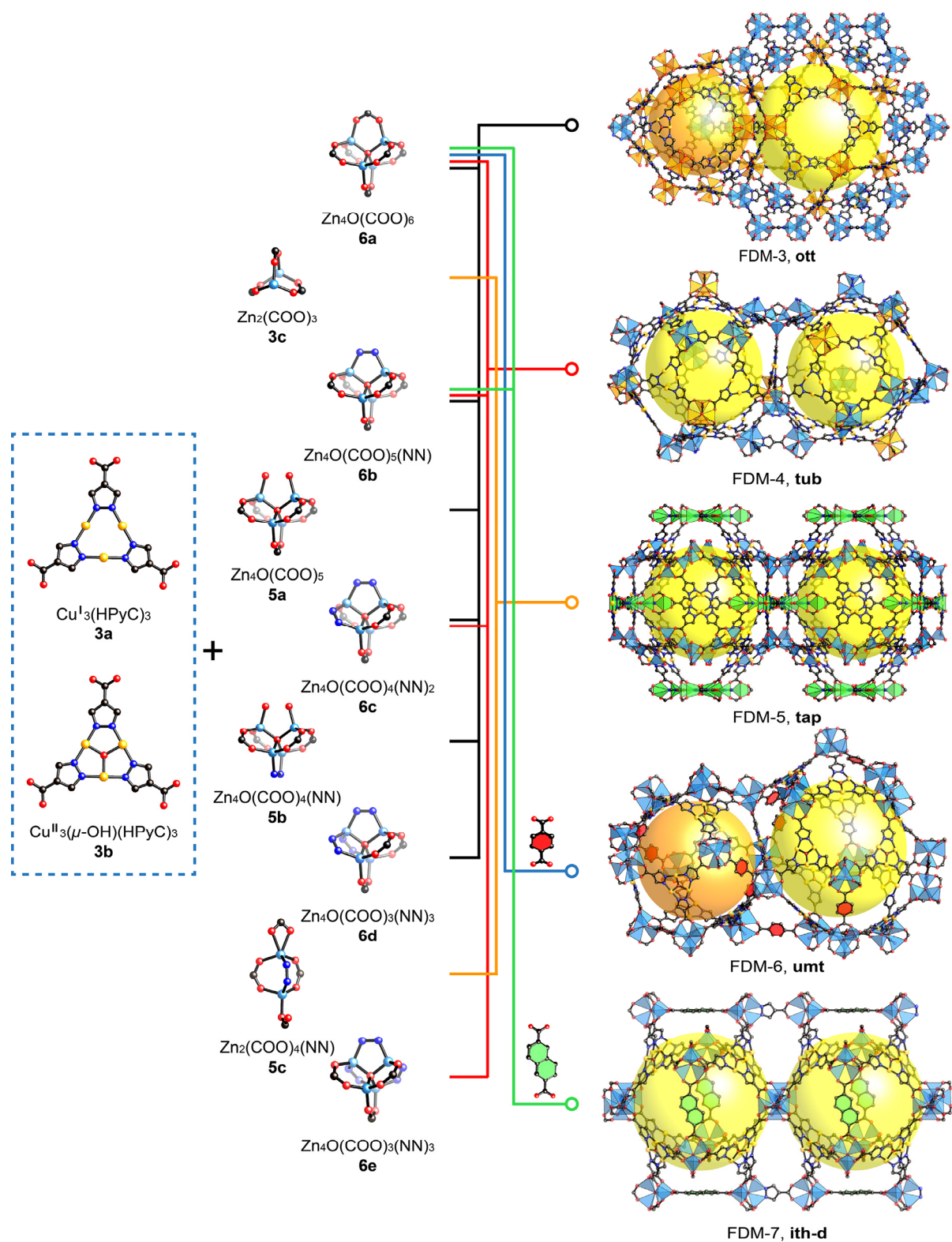


Figure 1. Construction of multicomponent FDM-3-7 using SBUs with distinct geometries. By employing triangular $\text{Cu}_3(\text{HPyC})_3$ (3a) or $\text{Cu}^{\text{II}}_3(\mu\text{-OH})(\text{HPyC})_3$ (3b), $\text{Zn}_2(\text{COO})_3$ (3c), square pyramidal $\text{Zn}_4\text{O}(\text{COO})_4\text{R}$ (5a, 5b), triangular bipyramidal $\text{Zn}_2(\text{COO})_4(\text{NN})$ (5c), and octahedral $\text{Zn}_4\text{O}(\text{COO})_3\text{R}_3$ (6a-6e), five multicomponent MOFs with different topologies were synthesized. Mesopores in FDM-3-7 are shown as yellow and orange spheres. R = COO or NN.

blocks have achieved complex MOFs with as many as four components. All four MOFs feature micropores and mesopores with Brunauer-Emmett-Teller (BET) surface area of

as high as $3728 \text{ m}^2 \text{ g}^{-1}$, despite the short linker used. The triangular building units in these MOFs undergo modulated redox reactions between $\text{Cu}_3(\text{PyC})_3$ and $\text{Cu}^{\text{II}}_3(\mu\text{-$

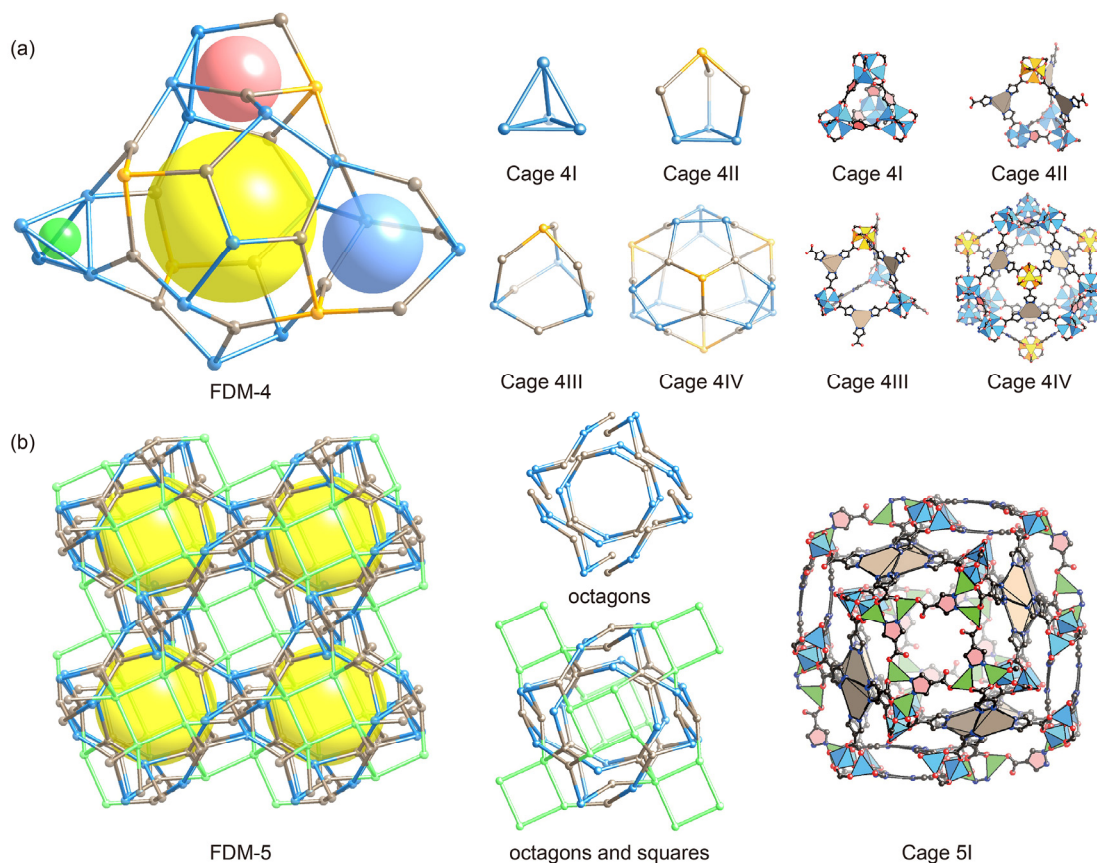


Figure 2. Topological and cage analysis of FDM-4 and FDM-5. (a) FDM-4 has four kinds of cages arranged in the new **tub** topology. (b) In FDM-5 with the new **tap** topology, six octagons were connected by six squares to form one cage with self-penetrated surface.

OH)(PyC)₃(OH)₃ reversibly without changing the underlying geometries of the units, as monitored by single crystal crystallography and X-ray photoelectron spectroscopy. Complete oxidation of CO to CO₂ and size selective oxidation of aromatic alcohols demonstrated the Cu(I) sites' high activities in both solid-gas and solid-solution interfaces. Furthermore, the facile interchangeability of Cu(I)/Cu(II) in these MOFs was investigated by their remarkable catalytic performances in H₂O₂ decomposition. Overall, the MOF designing principles presented here provide a systematic approach to program multiple components into one single crystal with high porosity; by further investigating the electronic communications between the precisely arranged components, these redox-active MOFs promise emerging catalytic properties.

RESULTS AND DISCUSSION

Synthesis of Multicomponent MOFs with New Topologies Using Metalloligand Strategy. The trinuclear complex entities, such as [Cu^I₃(HPyC)₃] (**3a** in Figure 1) or [Cu^{II}₃(μ-OH)(HPyC)₃]²⁺ (**3b** in Figure 1), could act as tri-topic carboxylate-based building blocks in MOF synthesis. With a spacer expansion of 3.3 Å along three directions compared to 1,3,5-benzenetricarboxylic acid (H₃BTC), this metalloligand made from H₂PyC allows to make MOF

structures with higher porosity. Furthermore, unlike another frequently used organic linker, 1,3,5-tris(4-carboxyphenyl)benzene (H₃BTB), all the carboxylates in the Cu-based metalloligand are in coplanar conformation, making the construction of new MOFs with high symmetry more feasible. Most importantly, H₂PyC is capable of separating and organizing different metal ions into SBUs with distinct geometries in a one-pot reaction, which was demonstrated previously in FDM-3 synthesis.^{6f} Recently, we have further explored the metalloligand strategy, and successfully constructed a series of MOFs with multiple components based on the trinuclear Cu-based building blocks.

Experimentally, by carefully controlling the mixed metal ratio of Zn and Cu in the solution with H₂PyC, colorless single crystals of FDM-4 (FDM = Fudan materials, Figure 1 and 2a) were synthesized solvothermally (see the Supporting Information (SI)). Single crystal X-ray diffraction (SXRD) reveals that FDM-4 crystallizes in the hexagonal non-centrosymmetric space group *P6₃mc* (Table S2). In FDM-4, Cu ions only coordinate with the pyrazolates to form the triangular metalloligands, while Zn ions coordinate with all the carboxylates and some additional pyrazolates. Thus, the network consists of octahedral SBUs based on Zn₄O(COO)₆ but with four variations (SBU **6a–6c**, and **6e** in Figure 1), and a triangular SBU **3a** (Figure 1). This

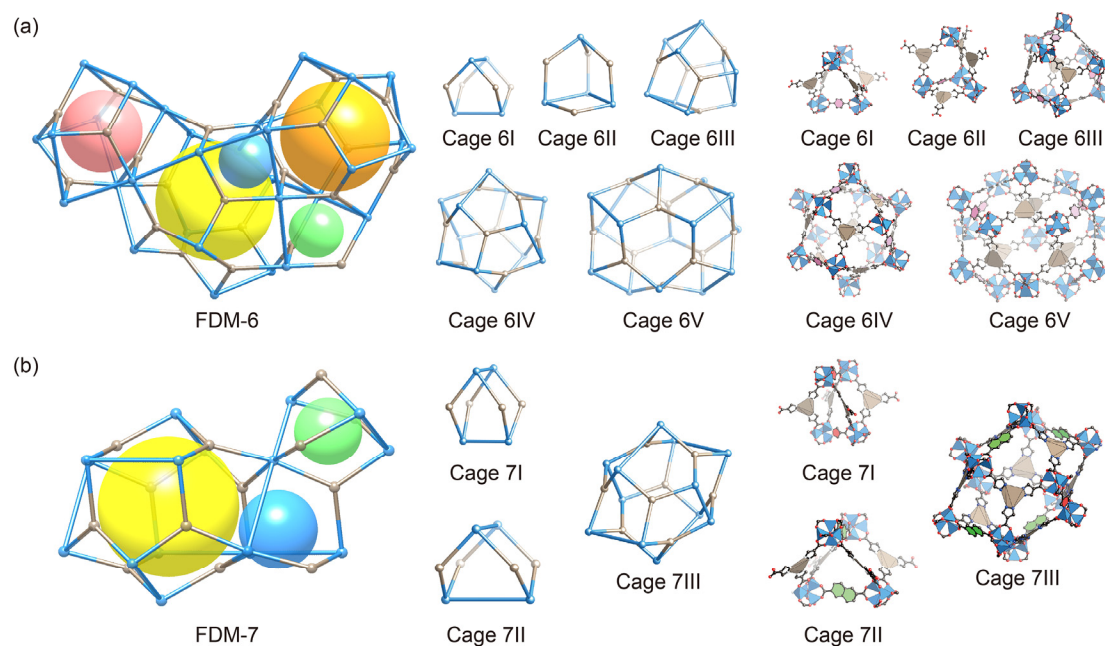


Figure 3. Topological and cage analysis of FDM-6 and FDM-7. (a) FDM-6 features five kinds of cages, and (b) FDM-7 has three kinds of cages in the network.

(3,6,6)-coordinated network possesses four kinds of polyhedral cages (Figure 2a). A small tetrahedral cage (Cage 4I) with the size of 5.2 Å is built with four octahedral SBUs as the nodes, and six PyC linkers as the edges. Both Cage 4II and Cage 4III use the Cu-based triangular SBUs (grey in Figure 2a) and two kinds of topologically distinct Zn-based octahedral SBUs (gold and blue in Figure 2a) as the nodes, with cage sizes of 7.2 Å and 11.4 Å, respectively. Interestingly, Cage 4II and 4III can be viewed as the expanded version of Cage 4I by replacing three or six PyC edges with the metalloligands. The largest cage in FDM-4, Cage 4IV is surrounded by twelve pentagons and four hexagons, and is mesoporous with a pore diameter of 24.0 Å. FDM-4 has the same four types of cages with the mixed-linker MOF UMCM-3^{4b}, however the spatial arrangements of the four cages are different (Figure S1), resulting in a new topology named **tub** for FDM-4.

Adjusting the solvothermal reaction condition slightly, we observed the formation of colorless single crystals of FDM-5. FDM-5 belongs to the tetragonal space group $I4/m$ (Table S2). In addition to the SBU 3a, triangular $Zn_2(COO)_3$ (3c) and triangular bipyramidal $Zn_2(COO)_4(NN)$ (5c) building blocks were located in FDM-5 by SXRD (Figure 1 and 2b). Despite of the multiple building blocks (three kinds of SBUs and one kind of linker) in FDM-5, it features only one type of porous cage. The surface of this cage is surrounded by six octagons composed of 3a and 3c, and they are further bridged by six squares using 5c as the nodes (Figure 2b). Interestingly, the stacking of the metalloligands 3a with each other (Cu–Cu distance of 3.52 Å from neighboring 3a, see Figure S2) and the noncoplanarity of the octagons make the framework self-penetrated (Figure 2b). With the inner size of the mesoporous Cage 5I

being 20.6×34.3 Å, the topology of the (3,3,5)-coordinated FDM-5 is unprecedented **tap**.

Synthesis of Multicomponent MOFs by Metalloligand and Organic Ligand Mixing. The FDM-4 and FDM-5 show examples of making multicomponent MOFs with new topologies by combining (i) the versatility in constructing Zn-based SBUs with distinct geometries and (ii) the straightforwardness in obtaining rigid Cu-based metalloligands with H_2PyC only as the ligand. However, whether the metalloligand strategy applies to systems involving H_2PyC and another organic linker remains unexplored, on account of the difficulties in consolidate two types of linkers (organic ligand and metalloligand) into one crystallization process simultaneously. Addressing this challenge, we synthesized FDM-6 and FDM-7 by introducing a second organic linker (1,4-benzenedicarboxylic acid (H_2BDC) for FDM-6 and 2,6-naphthalenedicarboxylic acid ($2,6-H_2NDC$) for FDM-7) into the reactions with Cu, Zn, and H_2PyC (Figure 1 and 3). In FDM-6 (Table S2), each octahedral 6a is coordinated with four triangular 3b and two BDC, resulting in a framework isorecticular to (3,6)-coordinated UMCM-2^{4a} with a topology of **umt**. In FDM-6, the ratio of the SBU 3b–6a distance (9.74 Å) to the SBU 6a–6a distance (13.02 Å) is 1:1.34, as determined by the length of PyC and BDC. This value is almost the same as the corresponding edge lengths ratio in UMCM-2 (1:1.37). In addition to the length ratio match, the identical geometry of the metalloligand in FDM-6 and the BTB in UMCM-2 has guided both structures to be assembled in the same topology. Crystallized in a hexagonal space group $P6_3/m$, FDM-6 features extraordinary five kinds of cages, the microporous Cages 6I–6III (7.0, 8.8, and 13.0×19.0 Å in cage sizes, respectively) and the mesoporous Cages 6IV–6V (20.2×23.4 and 20.4×31.0 Å in cage sizes, respectively). The dodecahedral Cage 6IV

has eight **6a** and twelve **3b** as the nodes, and Cage **6V** is a pentadecahedron with three hexagons and twelve pentagons.

On the other hand, FDM-7 (Figure 1 and **3b**, Table S2) contains the metalloligand (**3b**), one octahedral SBU with two variations (**6a** and **6b**), and two kinds of linear dicarboxylic acids with different lengths (PyC and NDC) in the network. Specifically, PyC has two roles in the FDM-7 construction: (i) participating in the formation of the triangular metalloligand, and (ii) serving as the linear ditopic linker. Indeed, PyC also has this dual role in FDM-3-5, whereas PyC in FDM-6 is only involved in the metalloligand construction. As a result, the arrangement of these four distinct components in order creates spontaneously three different types of cages in FDM-7. Cage **7I** and **7II** have the same faces, however, the edge length difference between PyC and NDC has created pores with different shapes (7.2×7.2 and 5.2×11.2 Å). The largest cage in FDM-7, Cage **7III** with the size of 18.4×21.6 Å, is the same [5¹²] tiling with the dodecahedral Cage **6IV**. This quaternary MOF is analogous to MOF-205^{4c} and MUF-7^{4d} with **ith-d** topology, however it avoids the use of costly tricarboxylic acid such as H₃BTB. Overall, the construction of three-component FDM-6 and four-component FDM-7 has expanded the metalloligand strategy to mixed linker system successfully. It can be concluded that the metalloligand and the organic linker share similar assembly kinetics under common MOF synthesis conditions, and could be rationally incorporated into multicomponent MOFs with high complexity in single phase.

It should be emphasized that, for the synthesis of FDM-3-7, the ratio between $\text{Cu}(\text{NO}_3)_2 \cdot 3\text{H}_2\text{O}$ and H_2PyC in the starting material was kept at around 1:2, and the concentration of $\text{Zn}(\text{NO}_3)_2 \cdot 6\text{H}_2\text{O}$ is at least 15 times higher than $\text{Cu}(\text{NO}_3)_2 \cdot 3\text{H}_2\text{O}$. This is to make sure that all the Cu ions coordinate with the pyrazolates, but not with the carboxylates. In general, a higher concentration of Cu ion may lead to the formation of MOF-325 as the by-product, which is based on the metalloligand **3b** and the $\text{Cu}_2(\text{COO})_4$ SBU. Under the optimized condition, we were able to synthesize FDM-3-7 all in pure phases, as evidenced by the powder X-ray diffraction (PXRD) analysis (Figure S3-S6).

Mesoporosity of FDM-4-7 Based on Short Struts. As can be seen from the single crystal structures, the mesoporous Cages **4IV**, **5I**, **6IV**, **6V**, and **7III** in FDM-4-7 contribute to the mesoporosity of the MOFs. To evaluate the porosity of these MOFs, we measured the N₂ adsorption isotherms of the activated samples at 77 K (Figure 4, see SI for the sample activation procedures). The BET surface areas of FDM-4-7 are 3393, 1067, 3728, and 3423 m² g⁻¹, respectively. We provide the complete pore analysis in Table 1 and Figure S7-S10, and here we describe the particular of FDM-6 containing five different types of cages as an illustrative example. With a Langmuir surface area of 4269 m² g⁻¹, FDM-6 has a high calculated void percentage of 82% based on the crystal structure, and the pore volume is 1.43 cm³ g⁻¹ based on the isotherm. FDM-6's void percentage ranks in the same category with several benchmark MOF materials, such as MOF-5 (79%), MIL-101 (81%), and MOF-

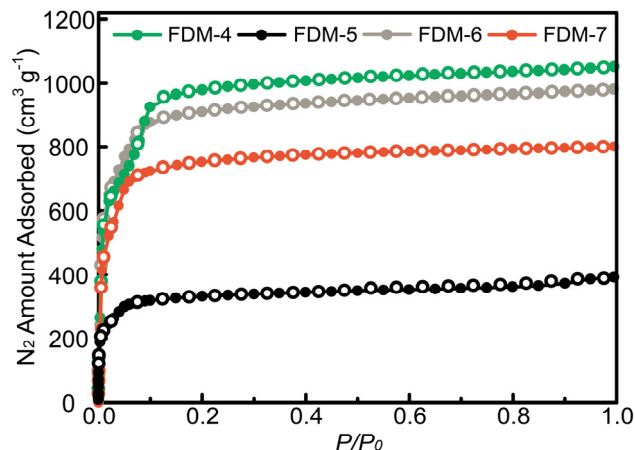


Figure 4. Low-pressure N₂ adsorption isotherms of FDM-4-7 at 77 K. Solid symbols represent adsorption, while open symbols represent desorption.

177 (83%).^{4c} In the pore size distribution profile (Figure S9), two distinct ranges (micropores with diameters of 1.0-1.5 nm and mesopores at 2.0-3.1 nm) were observed, corresponding to the microporous Cages **6I-III** and mesoporous Cages **6IV-V**. Despite the length of PyC being only 4.2 Å, consolidating two metal ions with distinct coordination preference and geometries into complex MOFs has made these structures mesoporous with high surface areas.

Oxidation and Reduction of Cu in the Triangular Building Blocks. Interestingly, all the FDM-4-7 crystals are colorless when they were firstly crystallized in capped vials (Figure 5a), indicating that Cu(II) ions from cupric nitrate were reduced during the synthesis, and the Cu in these as-synthesized MOF structures is monovalent. A close re-examination of the previously reported FDM-3 recorded the same observation. Reduction of Cu(II) to Cu(I) is not rare in MOF synthesis, and possibly assisted by the solvents as the reductant.^{9f,11} However, to our surprise, after loosening the vial caps, the crystal color transformed to light blue immediately for all five MOFs, suggesting that some Cu(I) in the framework were oxidized to Cu(II) upon contacting with ambient air (Figure 5b). In view of this, we performed the FDM-6 synthesis in a sealed tube filled with N₂. The formed FDM-6 crystals keep colorless for weeks until the tube is opened, indicating that the Cu(I) in the MOF structure is stable until it contacts with air.

The fast oxidation addresses a challenge in the accurate structure determination of the Cu-based SBUs in these MOFs by SXRD. Depending on the length of air contact time before and during data collection, partial or full oxidation of Cu(I) occurs, and therefore different SBUs (**3a** or **3b** in Figure 1) were presented. In the reported structures from SXRD, FDM-4 and FDM-5 feature the **3a** units in the frameworks; on the other hand, FDM-6 and FDM-7 has the **3b** as the building blocks, in which the square-planar coordination geometry of Cu(II) is fulfilled by OH⁻ as the terminal ligand. However, considering all the pristine crystals being colorless, we propose that the as-synthesized FDM-3-7 have the $\text{Cu}^1_3(\text{PyC})_3$ units as the building blocks, and

Table 1. Porosity data of activated FDM-3-7.

Compound	RCSR code	Crystal density (g cm ⁻³)	A _{BET} (m ² g ⁻¹)	A _{Lang} (m ² g ⁻¹)	V _p (cm ³ g ⁻¹)	Calculated void percentage (%)	Reference
FDM-3	ott	0.59	2585	2760	1.19	81	(6f)
FDM-4	tub	0.67	3393	3826	1.53	83	This work
FDM-5	tap	1.05	1067	1085	0.57	68	This work
FDM-6	umt	0.61	3728	4269	1.43	82	This work
FDM-7	ith-d	0.68	3423	3863	1.17	81	This work

Crystal densities are based on the formulas including compensating ions. A_{BET} and A_{Lang} are the BET and Langmuir surface areas, respectively. V_p is the measured pore volume. Calculated void percentage (%) is based on the accessible pore volume simulated on the MOF skeleton structures by Materials Studio.

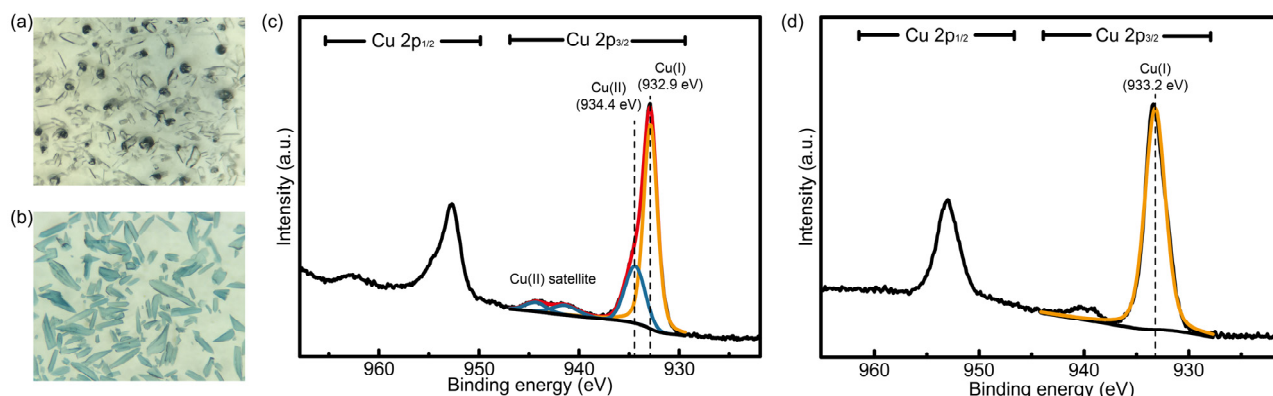


Figure 5. (a) Still image of the colorless as-synthesized FDM-6 crystals; (b) still image of FDM-6 crystals immediately after contacting with air; (c) XPS profile of FDM-6 dried under vacuum at room temperature; (d) XPS profile of FDM-6 activated under vacuum at 200 °C.

they were oxidized to Cu^{II}₃(μ-OH)(PyC)₃ upon exposed to the ambient air.

Based on the single crystal structures, CHN elemental analysis, and ICP-AES (see SI for details), we conclude formulas of all the as-synthesized MOFs based on Cu^I₃(PyC)₃, fully-oxidized MOFs based on Cu^{II}₃(μ-OH)(PyC)₃, and mixed-charge MOFs based on Cu^I_xCu^{II}_{3-x}(μ-OH)_{1-x/3}(PyC)₃(OH)_{3-x} (x = 0-3) in Table S1. For example, the formula of the as-synthesized FDM-4 is {(Zn₄O)₅[Cu^I₃(PyC)₃]₆(PyC)₆·[Zn(OH)₂(H₂O)₂]₆. When FDM-4 is fully oxidized, the formula changes to {(Zn₄O)₅[Cu^{II}₃(μ-OH)(PyC)₃]₆(PyC)₆(OH)₁₈·[Zn(OH)(H₂O)₃]₆. It is noteworthy that one OH⁻ from the isolated Zn-based complex which stays in the pores to compensate the charge but could not be located by SXRD, is substituted with H₂O to keep the MOF structure neutral upon oxidation.

X-ray photoelectron spectroscopy (XPS) is a powerful tool to examine the valence of Cu in FDM-3-7, and it shows mixed charge for all five MOFs even with minimum exposure to the air during the MOF drying process (wash with *N,N*-dimethylformamide (DMF), solvent exchange with CH₂Cl₂, followed by vacuum dry at room temperature). Specifically, as shown in Figure 5c, an intense asymmetrical Cu 2p_{3/2} photoelectron peak along with satellite peaks indicate mixed valence state of Cu in FDM-6. This peak can be deconvoluted into two contributions located at 932.9

and 934.4 eV, corresponding to Cu(I) 2p_{3/2} and Cu(II) 2p_{3/2}, respectively. Integration of the Cu(I) 2p_{3/2} peak, and Cu(II) 2p_{3/2} peak with Cu(II) satellite peaks (941.4 and 944.3 eV) gives the calculated ratio of Cu(I):Cu(II) being ~2.0:1.0 in FDM-6. Other investigated MOFs also show mixed valence state of Cu, with the ratios of Cu(I):Cu(II) in FDM-3, -4, -5, and -7 being ~1.1:1.9, 2.2:0.8, 1.0:2.0, and 1.3:1.7, respectively (Figure S11, S13, S15, and S17). These results suggest that FDM-3-7, featuring the same Cu-based SBUs, but with completely different spatial arrangement of SBUs and distinct local electronic structures around these SBUs, show varied oxidation rate even the same sample drying procedure with similar air exposure time was applied. Interestingly, complete oxidation of these MOFs within a short period could be achieved by adding additional oxidants, as indicated by the appearance of only Cu(II) 2p_{3/2} peaks (933.4 eV in Figure S19, 933.6 eV in Figure S20, and 933.7 eV in Figure S21) in the cases of FDM-4 and FDM-6 oxidized with H₂O₂, and FDM-3 oxidized with Ag⁺, respectively.

Most of the reports on MOFs with Cu-based triangular SBUs suggest the oxidation state of Cu being either 2+ or 1+, with 2+ dominant in the literatures. Few structures made from bipyrazole show very slow oxidation of Cu(I) in the air, as indicated by the mild color change of the crystals.^{9a,12} However, FDM-3-7 are the first MOF examples where the oxidation of Cu(I) happens rapidly and can be

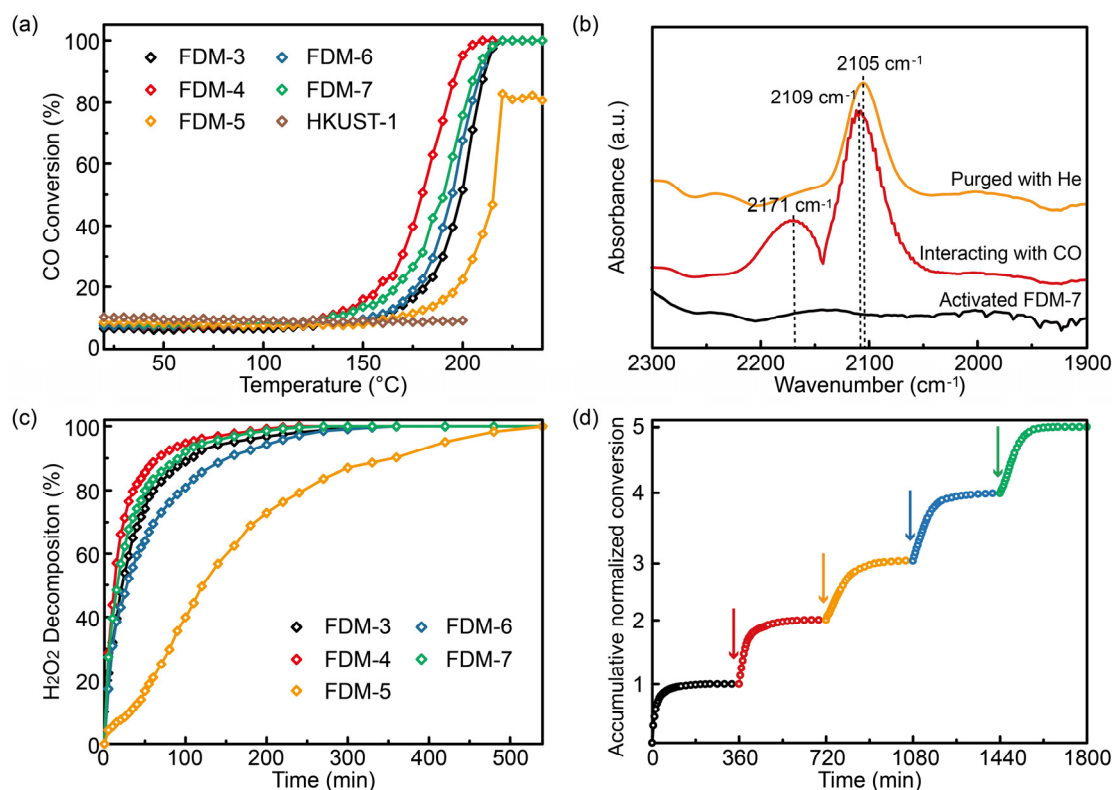


Figure 6. (a) CO conversion as a function of reaction temperature over activated FDM-3–7 and HKUST-1. (b) DFRITS of activated FDM-7 under He flow (black), after interacting with CO (red), and after purged with He (yellow). (c) Results on H₂O₂ decomposition catalyzed by activated FDM-3–7 at room temperature. (d) Performance on five sequential batches of H₂O₂ decomposition over activated FDM-4 at room temperature. The arrows indicate injection of 1 mL H₂O₂ without any regeneration with 6-h interval each time.

quantatively monitored by XPS. In FDM-3–7, the Zn(II)–carboxylate coordination bonding withdraws electrons from the PyC linker, which makes the Cu(I) on the other end of PyC more prone to be attacked by the nucleophiles, and thus facilitates the activation of the dioxygen molecules and the oxidation of Cu(I).¹³ With the distance of N from pyrazole and O from carboxylic acid as short as 4.2 Å, the PyC bridging ligand between two metals allows substantial electronic communication, and thus influence the redox behavior of each of the Cu(I) site in the framework. The multicomponent nature of these MOFs provides an ideal platform to further fine-tune the redox properties of the structures by controlling their arrangements in three-dimensional spaces and studying the electronic effects of each of the building units.

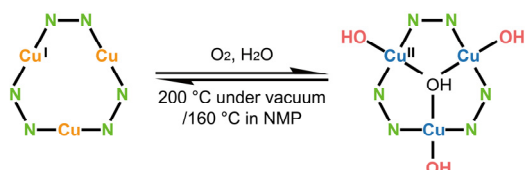
Interestingly, when the partially oxidized FDM-3–7 were activated by heating at 200 °C under vacuum, the crystal color turned light yellow for all five MOFs. The XPS spectra show that the percentage of Cu(I) in Cu ions in these MOFs increased after the activation, indicating reduction of Cu(II) to Cu(I).¹⁴ Specifically, as shown in Figure S12, S14, 5d, and S18, thermally activated FDM-3, -4, -6, and -7 show only intense sharp Cu(I) 2p_{3/2} peaks at 933.0, 932.6, 933.2, and 933.0 eV without satellite peaks, respectively, implying all Cu(II) are reduced to Cu(I). For FDM-5, the reduction is not complete after thermal treatment, despite the increase in the percentage of Cu(I) ions from ~33% to ~73% (Figure

S16). What is more, the reduction could be triggered not only by heating, but also by mild reductive solvent. All the partially oxidized MOFs could turn back to colorless upon heating in *N*-methyl-2-pyrrolidone (NMP) at 160 °C for less than 10 min, indicating complete reduction to Cu(I). With the conversion from SBU **3a** to **3b**, and back to **3a** along the oxidation and reduction, the frameworks of FDM-4–7 still retain their crystallinity with the same respective unit cell parameters, as validated by the coincidence of the experimental PXRD patterns of the thermally activated samples with their simulation (Figure S3–S6).

We picked FDM-6 to further study the reversibility of the Cu(I)/Cu(II) transformation in these frameworks. Within our expectation, exposing thermally activated FDM-6 to the air results in the color change to blue again. However, compared to the as-synthesized FDM-6, the activated sample is more resisted to be oxidized in ambient air, as evidenced by the apparent slower color change of the crystals. This is possibly due to the lacking of nucleophiles such as water in the pores. To prove this, we placed the light yellow crystals of reduced FDM-6 in a glovebox filled with oxygen, crystal color remained unchanged, confirming that H₂O is needed to convert Cu(I) to Cu(II) upon contacting with O₂. In summary, as proposed in Scheme 1, the linear coordinated Cu(I) in Cu^I₃(PyC)₃ is oxidized under O₂ and H₂O, and the trinuclear SBU evolves into Cu^{II}₃(μ-OH)(PyC)₃(OH)₃. This reaction can be reversed by heating

under vacuum or with mild reducing agent (see the SI for full equation).

Scheme 1. The interchangeability of Cu valences in the frameworks of FDM-3-7.



Oxidation of Carbon Monoxide by FDM-3-7. The study of carbon monoxide oxidation over Cu-based catalysts has its significance in the exhaust emission control.¹⁵ Cu(I) is known to catalyze the oxidation of CO by the use of valence variation to seize or release oxygen readily.¹⁶ With all the Cu(I) sites accessible in the activated FDM-3-7, we investigated their catalytic activities in CO oxidation using a fix bed flow reactor. CO (1% in air) was passed through the bed after the MOFs were pretreated in He at 200 °C for 2 h, and the effluent gases were analyzed by GC. Figure 6a shows that the activated FDM-3-7 can catalyze the oxidation of CO, with complete conversion to CO₂ at ~210 °C for FDM-4, and ~220 °C for FDM-3, -6, and -7. The PXRD of these four MOFs after CO oxidation at up to 240 °C showed that all the peaks corresponded to the pristine MOF structures (Figure S23, S24, S26, and S27), suggesting the MOFs retain their structures during the reactions. Furthermore, no peak from either Cu₂O or CuO was observed, confirming the catalytic active sites are the triangular Cu-based modules which are accessible to CO guests. In the case of the activated FDM-5, full conversion was not achieved, probably due to the relative instability of the bimetallic Zn₂(COO)₃ (SBU 3c) and Zn₂(COO)₄(NN) (SBU 5c) under high temperature, as evidenced by the early weight loss in TGA (Figure S22) and peak disappearance in PXRD after CO oxidation (Figure S25).

The temperature required for 50% CO conversion ($T_{1/2}$) is 200, 180, 215, 195, and 190 °C for FDM-3-7, respectively. Our control studies on Cu^I₂(COO)₄ based HKUST-1¹⁷ activated by heating at 200 °C under vacuum shows no activity at 200 °C. Although HKUST-1 activated with higher temperature (230 and 250 °C) have shown CO oxidation activities below 200 °C previously,¹⁸ it is unclear if the activity is from the reduced Cu(I) in the framework¹⁹ or Cu₂O from the decomposition of HKUST-1.^{14b,20} Overall, compared to HKUST-1 and a reported copper pyrazolotecarboxylate MOF²¹ with redox-inactive Cu(II)-based units under similar activation methods, lower temperature was recorded for 100% CO conversion using the MOFs presented. We conclude that the elevated performance is due to the high density of Cu(I) sites in the framework, and their aptness in valence variation during the conversion. In addition, high surface areas and large pore openings of mesoporous FDM-3-7 guarantee the accessibility of active sites, and free diffusion of CO, O₂, and CO₂.

The interaction between CO and Cu sites in FDM-3-7 were further studied by *in situ* diffuse reflectance infrared

Fourier transform spectroscopy (DRIFTS). Figure 6b shows the DRIFTS of the FDM-7 after three stepwise treatments (preheated at 200 °C for 2 h under He, exposed to 5 v.% CO flow for 30 mins, and purged with He for 15 min after CO exposure), and the DRIFTS for other MOFs are provided in Figure S28-S31. After exposing FDM-7 to CO, two peaks at 2171 and 2109 cm⁻¹ were observed. Upon purging with He, the peak at 2171 cm⁻¹ disappears, and the peak at 2109 cm⁻¹ shifts slightly to 2105 cm⁻¹. It is known that CO adsorption on Cu²⁺ or Cu⁰ is very weak and could be easily removed by purging at room temperature, thus the remaining peak at 2105 cm⁻¹ can be assigned to the stretching vibration of the typical C-O bond after CO chemisorption on Cu(I) sites^{8a,20,22}. For FDM-3-6, similar DRIFTS results were obtained, confirming the strong interaction between the CO and Cu(I) sites in the MOFs, and the subsequent CO activation.

H₂O₂ Decomposition Catalyzed by FDM-3-7. The interchangeability of Cu valences in FDM-3-7 drives us to further evaluate their catalytic performances in H₂O₂ decomposition. Transition metal catalyzed decomposition of H₂O₂ into H₂O and O₂ usually involves redox-active species, such as Cu(II)/Cu(I) sites in Cu-amine complex or Fe(III)/Fe(II) sites in iron oxide.²³ When H₂O₂ (30% in H₂O, 1.0 mL) was added to the activated FDM-3 (~0.1 mmol Cu sites) in DMF, violent O₂ bubbles emerge from the surface of the MOF crystals immediately and the gas evolving process continues for up to 24 hours (Video S1 in the SI). FDM-4-7 show similar catalytic activities in H₂O₂ decomposition with activated FDM-3, confirming the decomposition is catalyzed by the same Cu-based triangular building blocks. In contrast, experiment performed on activated HKUST-1 shows no O₂ released from the crystals (Video S2 in the SI), indicating that the decomposition of H₂O₂ cannot be catalyzed by Lewis acidic Cu(II) sites as in HKUST-1, but by the redox-active Cu(II)/Cu(I) sites as in FDM-3-7. It is worth noting that the crystals color turn darker at the initial H₂O₂ decomposition stage, indicating some Cu(I) were possibly oxidized to Cu(II) by the O₂ released.

With the help of stirring, H₂O₂ decomposition rate can be accelerated to less than 6 hours for the aforementioned reaction, with ~100% H₂O₂ conversion observed by the time interval measurement of the O₂ volume (Figure 6c). We picked the data from 50 to 100 min after H₂O₂ contacted with the five MOFs to look at the kinetics of the reaction, for the reasons that (i) during this period the effect of diffusion barrier of H₂O₂ into the MOF pores can be considered as constant, and (ii) a good amount of released O₂ keeps the relative error of the measured O₂ volume small. As shown in Figure S32, pseudo-first order kinetic patterns were observed for all the H₂O₂ decomposition catalyzed by five different MOFs. The k_{obs} of the reactions are $(1.64 \pm 0.07) \times 10^{-2}$, $(2.00 \pm 0.06) \times 10^{-2}$, $(0.66 \pm 0.02) \times 10^{-2}$, $(1.24 \pm 0.04) \times 10^{-2}$, and $(1.77 \pm 0.07) \times 10^{-2} \text{ min}^{-1}$ for FDM-3-7, respectively. Furthermore, the systems still retain their activities for several batches without any regeneration process, as indicated by the full O₂ evolution upon injecting H₂O₂ in equal amounts every 6 h for FDM-4 (Figure 6d). After five sequential batches, assuming all Cu sites in FDM-4 are

active, each Cu site involves at least 500 cycles of rigorous H₂O₂ conversion without obvious decrease in the reaction rate. These MOFs lost their high crystallinity after H₂O₂ decomposition experiment according to PXRD (Figure S33), indicating possible structural amorphisation due to the frequent Cu valence interchange and H₂O coordination competition. However, the crystals remain their original shape after the catalysis (without stirring, Figure S34), suggesting the frameworks still hold their integrity. What is more, the reaction solution remain colorless and no precipitate forms upon addition of Na₂S into the supernatant, indicating no Cu from the framework is leached into the solution.

Pristine FDM-3-7 as Benzyl Alcohol Oxidation Catalysts. Complexes and MOFs based on Cu have been shown to catalyze the aerobic oxidation of benzyl alcohol.²⁴ One of the proposed mechanisms involving Cu(I) site includes its oxidation to Cu(II) by O₂, followed by the alcohol's oxidation to aldehyde by the Cu(II) species and co-catalyst.^{24a} The redox facility and accessibility of the Cu(I) sites is the key in achieving efficient catalysis. However, MOFs containing accessible and redox-active Cu(I) sites for alcohol oxidation are in scarce, with only one example of introducing Cu(I) sites by post-synthetic modification.^{24b} With Cu(I) sites decorating on the pore surfaces and taking up more than 19 wt% in the solids, FDM-3-7 were examined as the catalysts for the aerobic oxidation of benzyl alcohol in the open air at 70 °C by using 2,2,6,6-tetramethyl-1-piperidinyloxy (TEMPO) and *N*-methylimidazole (NMI) as co-catalysts, and the yields were checked by ¹H NMR. As shown in Table 2, without MOF catalyst, the reaction shows very low yield (2%); however, all the five pristine MOFs investigated show remarkable catalytic activities in its oxidation to benzaldehyde. Specifically, the yields of benzaldehyde are 98%, >99%, 62%, >99%, and 98% for the reactions catalyzed by activated FDM-3-7 in 24 h. The unsatisfactory yield in the case of FDM-5 is due to the smaller pore opening (with the aperture diagonal of 6.0 Å) and possible lower chemical stability. Indeed, a high yield of 70%, 83%, 84% and 87% were achieved for FDM-3, -4, -6 and -7 as catalysts within the first 12 h. The pores inside these MOFs allow free movement of benzyl alcohol in the crystals and close contact with the active Cu sites without any steric hindrance.

Pristine FDM-3-7 show great activities in the alcohol oxidation, although our preliminary studies on the PXRD reveal the solids lost their crystallinities after catalytic reactions. We understand that the participation of several Zn-carboxylate based SBUs (such as **3c** and **6a**) in these MOFs may raise chemical stability issues when they were applied as catalysts in the reactions with TEMPO and NMI. To elucidate the heterogeneous nature of the porous catalysts, we performed their substrate size selectivity studies under the same condition. 3,4,5-Trimethoxybenzyl alcohol (TMBA) was picked for its larger size (~9.5 × 9.2 Å) than benzyl alcohol (~6.0 × 4.3 Å). Based on the single crystal structures, FDM-3, -4, -6, and -7 have their pore openings all at ~11.0 Å, which restrain the free movement of TMBA inside the crystals to some extent. Consequently, drastic drop in the yields (13% for FDM-4 and 15% for FDM-6 in 24 h, Table 2)

was observed. These results suggest that the oxidation of benzyl alcohol mainly happens inside the MOF crystals rather than in homogeneous solutions; and the size and shape of TMBA molecules have made them (i) diffuse very slowly in the pores, and (ii) difficult to contact with the Cu active sites due to space restriction. Overall, the size and shape selectivity towards the substrates confirms the heterogeneous nature of the MOF catalysts, whose structural character still stands and pore accessibility still remains. With MOF building blocks for higher chemical stability available,²⁵ researches on new structures incorporating these accessible redox-active sites will provide materials with unparalleled catalytic performances.

Table 2. Aerobic oxidation of benzyl alcohol and TMBA using FDM-3-7.

Entry	Catalyst	Substrate	Time	Yield
1	/	benzyl alcohol	24 h	2%
2	FDM-3	benzyl alcohol	12 h	70%
3	FDM-3	benzyl alcohol	24 h	98%
4	FDM-4	benzyl alcohol	12 h	83%
5	FDM-4	benzyl alcohol	24 h	>99%
6	FDM-5	benzyl alcohol	24 h	62%
7	FDM-6	benzyl alcohol	12 h	84%
8	FDM-6	benzyl alcohol	24 h	>99%
9	FDM-7	benzyl alcohol	12 h	87%
10	FDM-7	benzyl alcohol	24 h	98%
11	FDM-4	TMBA	24 h	13%
12	FDM-6	TMBA	24 h	15%

CONCLUSION

In summary, the triangular copper pyrazolate building blocks provide a rational strategy to further explore the multiplicity of structural components in single MOFs, as demonstrated in mesoporous FDM-3-7 with up to four distinct constituents. Furthermore, the classic Cu(I)/Cu(II) redox activities of the trinuclear Cu-based modules²⁶ were inherited after they were apportioned in precise positions throughout the whole porous network. The catalytic performances of these redox-active multicomponent MOFs were verified by the oxidation of CO and aromatic alcohols, and the decomposition of H₂O₂. Akin to the multi-copper sites in natural enzymes, such as oxidases or oxygenases, the active sites in the MOFs with multiple components under synergy control present their potentials in precision catalysis.

ASSOCIATED CONTENT

Supporting Information

The Supporting Information is available free of charge on the ACS Publications website at DOI: 10.1021/

Synthetic and characterization procedures; PXRD, XPS, TGA, DRIFTS, and pore analyses of MOFs; CO oxidation, H₂O₂ decomposition, alcohol oxidation experiment details (PDF)

Crystallographic data for FDM-4-7 (CIF)
H₂O₂ decomposition video (AVI)

AUTHOR INFORMATION

Corresponding Author

*qwli@fudan.edu.cn

ORCID

Binbin Tu: 0000-0003-3800-6208

Qingqing Pang: 0000-0003-0580-8570

Huoshu Xu: 0000-0001-9027-0095

Xiaomin Li: 0000-0001-8931-0969

Qiaowei Li: 0000-0002-5987-9465

Notes

The authors declare no competing financial interest.

ACKNOWLEDGMENT

This work was supported by the National Natural Science Foundation of China (21571037), Shanghai Rising-Star Program (15QA1400400), and the Science & Technology Commission of Shanghai Municipality (14JC1400700, 16520710100, 16DZ2270100). The authors would like to thank Prof. Michael O’Keeffe for fruitful discussions and generous support to this work.

REFERENCES

- (1) (a) Li, H.; Eddaoudi, M.; O’Keeffe, M.; Yaghi, O. M. *Nature* **1999**, *402*, 276. (b) Kitagawa, S.; Kitaura, R.; Noro, S. *Angew. Chem., Int. Ed.* **2004**, *43*, 2334. (c) Férey, G. *Chem. Soc. Rev.* **2008**, *37*, 191. (d) Zhang, J.-P.; Zhang, Y.-B.; Lin, J.-B.; Chen, X.-M. *Chem. Rev.* **2012**, *112*, 1001. (e) Zhou, H. C.; Long, J. R.; Yaghi, O. M. *Chem. Rev.* **2012**, *112*, 673. (f) Furukawa, H.; Cordova, K. E.; O’Keeffe, M.; Yaghi, O. M. *Science* **2013**, *341*, 1230444.
- (2) (a) Eddaoudi, M.; Kim, J.; Rosi, N.; Vodak, D.; Wachter, J.; O’Keeffe, M.; Yaghi, O. M. *Science* **2002**, *295*, 469. (b) Kandiah, M.; Nilsen, M. H.; Usseglio, S.; Jakobsen, S.; Olsbye, U.; Tilset, M.; Larrabi, C.; Quadrelli, E. A.; Bonino, F.; Lillerud, K. P. *Chem. Mater.* **2010**, *22*, 6632. (c) Serra-Crespo, P.; Ramos-Fernandez, E. V.; Gascon, J.; Kapteijn, F. *Chem. Mater.* **2011**, *23*, 2565. (d) Deng, H.; Grunder, S.; Cordova, K. E.; Valente, C.; Furukawa, H.; Hmadeh, M.; Gándara, F.; Whalley, A. C.; Liu, Z.; Asahina, S.; Kazumori, H.; O’Keeffe, M.; Terasaki, O.; Stoddart, J. F.; Yaghi, O. M. *Science* **2012**, *336*, 1018. (e) Lu, W.; Wei, Z.; Gu, Z. Y.; Liu, T. F.; Park, J.; Park, J.; Tian, J.; Zhang, M.; Zhang, Q.; Gentile, T., III; Bosch, M.; Zhou, H. C. *Chem. Soc. Rev.* **2014**, *43*, 5561. (f) Chen, T.-H.; Popov, I.; Kaveevivitchai, W.; Miljanic, O. Š. *Chem. Mater.* **2014**, *26*, 4322.
- (3) (a) Kiang, Y.-H.; Gardner, G. B.; Lee, S.; Xu, Z.; Lobkovsky, E. B. *J. Am. Chem. Soc.* **1999**, *121*, 8204. (b) Seo, J. S.; Whang, D.; Lee, H.; Jun, S. I.; Oh, J.; Jeon, Y. J.; Kim, K. *Nature* **2000**, *404*, 982. (c) Wang, Z.; Cohen, S. M. *J. Am. Chem. Soc.* **2007**, *129*, 12368. (d) Haneda, T.; Kawano, M.; Kawamichi, T.; Fujita, M. *J. Am. Chem. Soc.* **2008**, *130*, 1578. (e) Wang, Z. Q.; Cohen, S. M. *Chem. Soc. Rev.* **2009**, *38*, 1315. (f) McDonald, T. M.; Mason, J. A.; Kong, X.; Bloch, E. D.; Gygi, D.; Dani, A.; Crocella, V.; Giordanino, F.; Odoh, S. O.; Drisdell, W.; Vlaisavljevich, B.; Dzubak, A. L.; Poloni, R.; Schnell, S. K.; Planas, N.; Lee, K.; Pascal, T.; Wan, L. F.; Prendergast, D.; Neaton, J. B.; Smit, B.; Kortrright, J. B.; Gagliardi, L.; Bordiga, S.; Reimer, J. A.; Long, J. R. *Nature* **2015**, *519*, 303. (g) Cohen, S. M. *J. Am. Chem. Soc.* **2017**, *139*, 2855.
- (4) (a) Koh, K.; Wong-Foy, A. G.; Matzger, A. J. *J. Am. Chem. Soc.* **2009**, *131*, 4184. (b) Koh, K.; Wong-Foy, A. G.; Matzger, A. J. *J. Am. Chem. Soc.* **2010**, *132*, 15005. (c) Furukawa, H.; Ko, N.; Go, Y. B.; Aratani, N.; Choi, S. B.; Choi, E.; Yazaydin, A. Ö.; Snurr, R. Q.; O’Keeffe, M.; Kim, J.; Yaghi, O. M. *Science* **2010**, *329*, 424. (d) Liu,

L.; Konstas, K.; Hill, M. R.; Telfer, S. G. *J. Am. Chem. Soc.* **2013**, *135*, 17731. (e) Chevreau, H.; Devic, T.; Salles, F.; Maurin, G.; Stock, N.; Serre, C. *Angew. Chem., Int. Ed.* **2013**, *52*, 5056. (f) Liu, L.; Telfer, S. G. *J. Am. Chem. Soc.* **2015**, *137*, 3901. (g) Furukawa, H.; Müller, U.; Yaghi, O. M. *Angew. Chem., Int. Ed.* **2015**, *54*, 3417.

(5) (a) Deng, H.; Doonan, C. J.; Furukawa, H.; Ferreira, R. B.; Towne, J.; Knobler, C. B.; Wang, B.; Yaghi, O. M. *Science* **2010**, *327*, 846. (b) Zhang, Y.-B.; Furukawa, H.; Ko, N.; Nie, W.; Park, H. J.; Okajima, S.; Cordova, K. E.; Deng, H.; Kim, J.; Yaghi, O. M. *J. Am. Chem. Soc.* **2015**, *137*, 2641.

(6) (a) Dincă, M.; Long, J. R. *J. Am. Chem. Soc.* **2007**, *129*, 11172. (b) Zheng, S.-T.; Wu, T.; Chou, C.; Fuhr, A.; Feng, P.; Bu, X. *J. Am. Chem. Soc.* **2012**, *134*, 4517. (c) Schoedel, A.; Cairns, A. J.; Belmabkhout, Y.; Wojtas, L.; Mohamed, M.; Zhang, Z.; Proserpio, D. M.; Eddaoudi, M.; Zaworotko, M. J. *Angew. Chem., Int. Ed.* **2013**, *52*, 2902. (d) Wang, L. J.; Deng, H.; Furukawa, H.; Gándara, F.; Cordova, K. E.; Peri, D.; Yaghi, O. M. *Inorg. Chem.* **2014**, *53*, 5881. (e) Li, M.; Li, D.; O’Keeffe, M.; Yaghi, O. M. *Chem. Rev.* **2014**, *114*, 1343. (f) Tu, B.; Pang, Q.; Ning, E.; Yan, W.; Qi, Y.; Wu, D.; Li, Q. *J. Am. Chem. Soc.* **2015**, *137*, 13456. (g) Zhai, Q.-G. Bu, X.; Mao, C.; Zhao, X.; Feng, P. *J. Am. Chem. Soc.* **2016**, *138*, 2524. (h) Han, Y.; Zheng, H.; Liu, K.; Wang, H.; Huang, H.; Xie, L.-H.; Wang, L.; Li, J.-R. *ACS Appl. Mater. Interfaces* **2016**, *8*, 23331.

(7) (a) Domenech, A.; Garcia, H.; Domenech-Carbo, M. T.; Llabres-i-Xamena, F. *J. Phys. Chem. C* **2007**, *111*, 13701. (b) Meilikhov, M.; Yusenko, K.; Fischer, R. A. *J. Am. Chem. Soc.* **2009**, *131*, 9644. (c) Bloch, E. D.; Murray, L. J.; Queen, W. L.; Chavan, S.; Maximoff, S. N.; Bigi, J. P.; Krishna, R.; Peterson, V. K.; Grandjean, F.; Long, G. J.; Smit, B.; Bordiga, S.; Brown, C. M.; Long, J. R. *J. Am. Chem. Soc.* **2011**, *133*, 14814. (d) Brozek, C. K.; Dincă, M. *J. Am. Chem. Soc.* **2013**, *135*, 12886. (e) Brozek, C. K.; Miller, J. T.; Stoian, S. A.; Dincă, M. *J. Am. Chem. Soc.* **2015**, *137*, 7495. (f) D’Alessandro, D. M. *Chem. Commun.* **2016**, *52*, 8957.

(8) Eddaoudi, M.; Moler, D. B.; Li, H.; Chen, B.; Reineke, T. M.; O’Keeffe, M.; Yaghi, O. M. *Acc. Chem. Res.* **2001**, *34*, 319.

(9) (a) Zhang, J.-P.; Kitagawa, S. *J. Am. Chem. Soc.* **2008**, *130*, 907. (b) Zhang, J.-X.; He, J.; Yin, Y.-G.; Hu, M.-H.; Li, D.; Huang, X.-C. *Inorg. Chem.* **2008**, *47*, 3471. (c) Procopio, E. Q.; Linares, F.; Montoro, C.; Colombo, V.; Maspero, A.; Barea, E.; Navarro, J. A. R. *Angew. Chem., Int. Ed.* **2010**, *49*, 7308. (d) Hou, L.; Shi, W.-J.; Wang, Y.-Y.; Wang, H.-H.; Cui, L.; Chen, P.-X.; Shi, Q.-Z. *Inorg. Chem.* **2011**, *50*, 261. (e) Tranchemontagne, D. J.; Park, K. S.; Furukawa, H.; Eckert, J.; Knobler, C. B.; Yaghi, O. M. *J. Phys. Chem. C* **2012**, *116*, 13143. (f) Wei, Z.-W.; Yuan, D.-Q.; Zhao, X.-L.; Sun, D.-F.; Zhou, H.-C. *Sci. China Chem.* **2013**, *56*, 418. (g) Xiao, Q.; Zheng, J.; Li, M.; Zhan, S.-Z.; Wang, J.-H.; Li, D. *Inorg. Chem.* **2014**, *53*, 11604. (h) Gao, W. Y.; Cai, R.; Pham, T.; Forrest, K. A.; Hogan, A.; Nugent, P.; Williams, K.; Wojtas, L.; Luebke, R.; Weselinski, L. J.; Zaworotko, M. J.; Space, B.; Chen, Y. S.; Eddaoudi, M.; Shi, X. D.; Ma, S. Q. *Chem. Mater.* **2015**, *27*, 2144.

(10) (a) Noro, S.; Miyasaka, H.; Kitagawa, S.; Wada, T.; Okubo, T.; Yamashita, M.; Mitani, T. *Inorg. Chem.* **2005**, *44*, 133. (b) Das, M. C.; Xiang, S.; Zhang, Z.; Chen, B. *Angew. Chem., Int. Ed.* **2011**, *50*, 10510.

(11) Lo, S. M. F.; Chui, S. S.-Y.; Shek, L.-Y.; Lin, Z.; Zhang, X. X.; Wen, G.-h.; Williams, I. D. *J. Am. Chem. Soc.* **2000**, *122*, 6293.

(12) (a) Grzywa, M.; Gefšner, C.; Denysenko, D.; Bredenkötter, B.; Gschwind, F.; Fromm, K. M.; Nitek, W.; Klemm, E.; Volkmer, D. *Dalton Trans.* **2013**, *42*, 6909. (b) Grzywa, M.; Bredenkötter, B.; Denysenko, D.; Spirk, S.; Nitek, W.; Volkmer, D. *Z. Anorg. Allg. Chem.* **2013**, *639*, 1461.

(13) Maji, S.; Lee, J. C.-M.; Lu, Y.-J.; Chen, C.-L.; Hung, M.-C.; Chen, P. P.-Y.; Yu, S. S.-F.; Chan, S. I. *Chem.—Eur. J.* **2012**, *18*, 3955.

(14) (a) Larsen, S. C.; Aylor, A.; Bell, A. T.; Reimer, J. A. *J. Phys. Chem.* **1994**, *98*, 11533. (b) Prestipino, C.; Regli, L.; Vitillo, J. G.; Bonino, F.; Damin, A.; Lamberti, C.; Zecchina, A.; Solari, P. L.; Kongshaug, K. O.; Bordiga, S. *Chem. Mater.* **2006**, *18*, 1337.

- 1
2
3 (15) Kummer, J. T. *Prog. Energy Combust. Sci.* **1980**, *6*, 177.
4 (16) Huang, T.-J.; Tsai, D.-H. *Catal. Lett.* **2003**, *87*, 173.
5 (17) Chui, S. S.-Y.; Lo, S. M.-F.; Charmant, J. P. H.; Orpen, A. G.;
6 Williams, I. D. *Science* **1999**, *283*, 1148.
7 (18) (a) Qiu, W.; Wang, Y.; Li, C.; Zhan, Z.; Zi, X.; Zhang, G.;
8 Wang, R.; He, H. *Chin. J. Catal.* **2012**, *33*, 986. (b) Kim, T.; Kim, D.
9 H.; Kim, S.; Kim, Y. D.; Bae, Y.-S.; Lee, C. Y. *Polyhedron* **2015**, *90*,
10 18.
11 (19) DeCoste, J. B.; Peterson, G. W. *Chem. Rev.* **2014**, *114*, 5695.
12 (20) Bordiga, S.; Regli, L.; Bonino, F.; Groppo, E.; Lamberti, C.;
13 Xiao, B.; Wheatley, P. S.; Morris, R. E.; Zecchina, A. *Phys. Chem.*
14 *Chem. Phys.* **2007**, *9*, 2676.
15 (21) Su, S.; Zhang, Y.; Zhu, M.; Song, X.; Wang, S.; Zhao, S.; Song,
16 S.; Yang, X.; Zhang, H. *Chem. Commun.* **2012**, *48*, 11118.
17 (22) Palomino, G. T.; Bordiga, S.; Zecchina, A. *J. Phys. Chem. B*
18 **2000**, *104*, 8641.
19 (23) (a) Salem, M. A.; Salem, I. A.; Gemeay, A. H. *Int. J. Chem.*
20 *Kinet.* **1994**, *26*, 1055. (b) Lin, S.-S.; Gurol, M. D. *Environ. Sci. Tech-*
21 *nol.* **1998**, *32*, 1417.
22
23
24
25
26
27
28
29
30
31
32
33
34
35
36
37
38
39
40
41
42
43
44
45
46
47
48
49
50
51
52
53
54
55
56
57
58
59
60 (24) (a) Hoover, J. M.; Ryland, B. L.; Stahl, S. S. *J. Am. Chem. Soc.*
2013, *135*, 2357. (b) Yuan, S.; Chen, Y.-P.; Qin, J.-S.; Lu, W.; Zou, L.;
Zhang, Q.; Wang, X.; Sun, X.; Zhou, H.-C. *J. Am. Chem. Soc.* **2016**,
138, 8912. (c) Kim, B. R.; Oh, J. S.; Kim, J.; Lee, C. Y. *Catal. Lett.*
2016, *146*, 734. (d) Miao, Z.; Luan, Y.; Qi, C.; Ramella, D. *Dalton*
Trans. **2016**, *45*, 13917.
(25) (a) Cavka, J. H.; Jakobsen, S.; Olsbye, U.; Guillou, N.; Lam-
berti, C.; Bordiga, C.; Lillerud, K. P. *J. Am. Chem. Soc.* **2008**, *130*,
13850. (b) Furukawa, H.; Gándara, F.; Zhang, Y.-B.; Jiang, J.; Queen,
W. L.; Hudson, M. R.; Yaghi, O. M. *J. Am. Chem. Soc.* **2014**, *136*,
4369. (c) Wang, K.; Lv, X.-L.; Feng, D.; Li, J.; Chen, S.; Sun, J.; Song,
L.; Xie, Y.; Li, J.-R.; Zhou, H.-C. *J. Am. Chem. Soc.* **2016**, *138*, 914.
(26) Hulsbergen, F. B.; ten Hoedt, R. W. M.; Verschoor, G. C.;
Reedijk, J.; Spek, A. L. *J. Chem. Soc., Dalton Trans.* **1983**, 539.

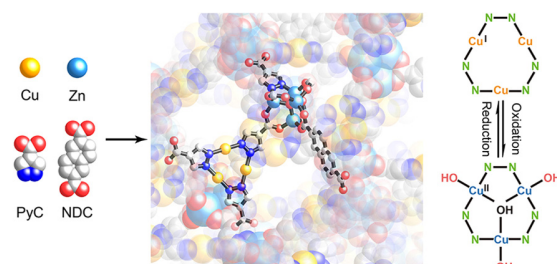
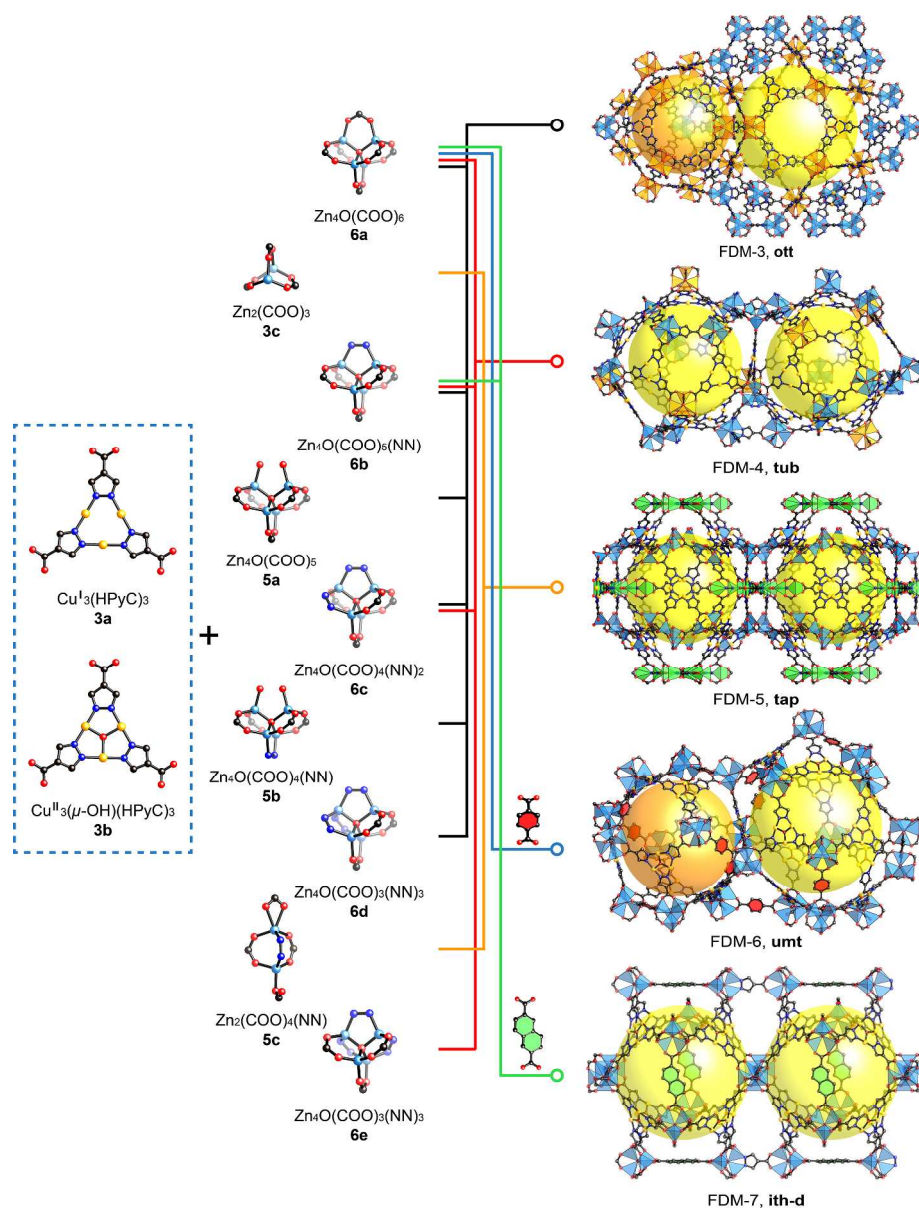
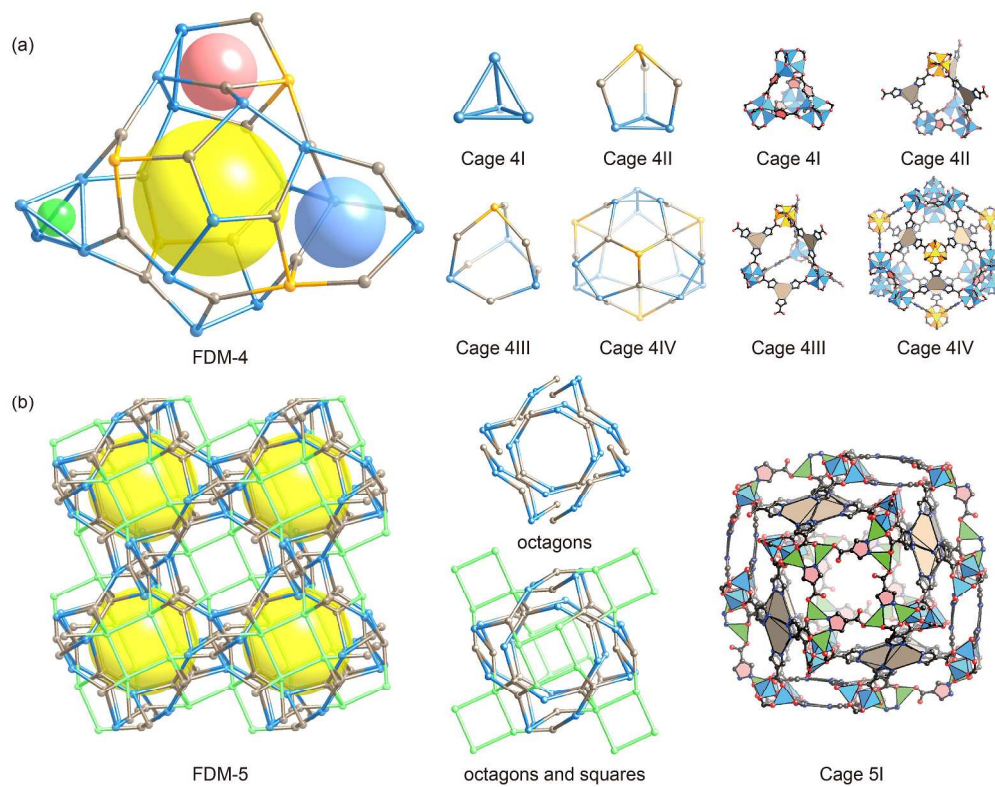


Table of Contents artwork



254x333mm (300 x 300 DPI)



33
34
35
36
37
38
39
40
41
42
43
44
45
46
47
48
49
50
51
52
53
54
55
56
57
58
59
60

Figure 2. Topological and cage analysis of FDM-4 and FDM-5. (a) FDM-4 has four kinds of cages arranged in the new **tub** topology. (b) In FDM-5 with the new **tap** topology, six octagons were connected by six squares to form one cage with self-penetrated surface.

254x197mm (300 x 300 DPI)

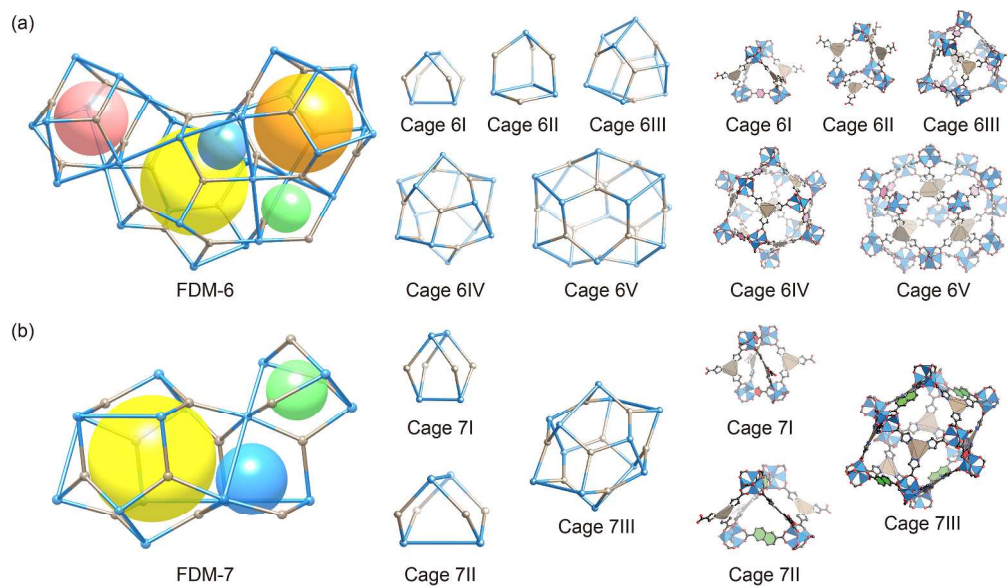


Figure 3. Topological and cage analysis of FDM-6 and FDM-7. (a) FDM-6 features five kinds of cages, and (b) FDM-7 has three kinds of cages in the network.

254x153mm (300 x 300 DPI)

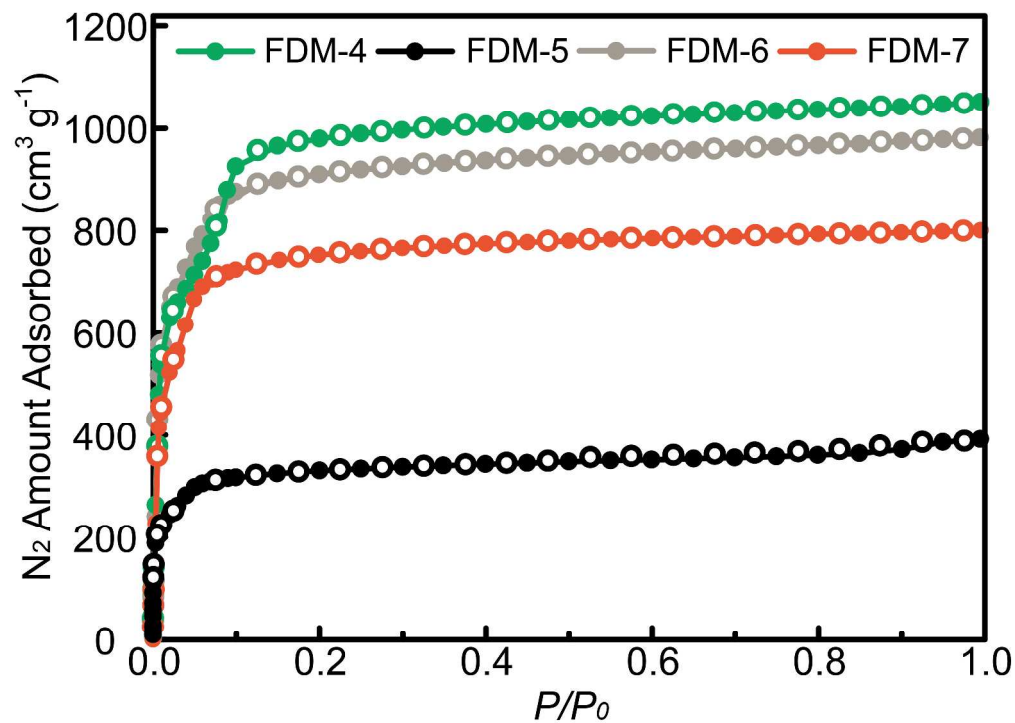


Figure 4. Low-pressure N₂ adsorption isotherms of FDM-4-7 at 77 K. Solid symbols represent adsorption, while open symbols represent desorption.

438x318mm (300 x 300 DPI)

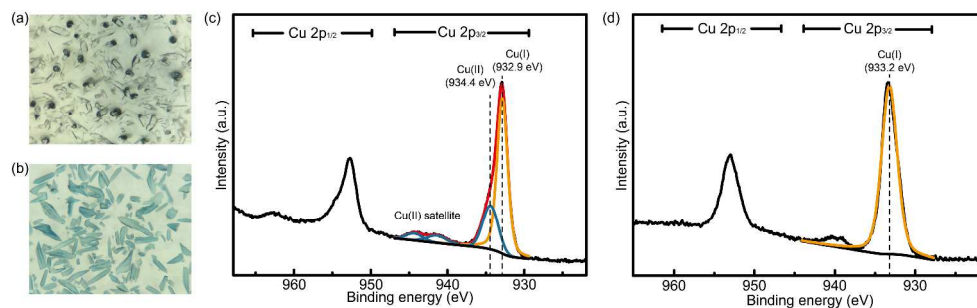


Figure 5. (a) Still image of the colorless as-synthesized FDM-6 crystals; (b) still image of FDM-6 crystals immediately after contacting with air; (c) XPS profile of FDM-6 dried under vacuum at room temperature; (d) XPS profile of FDM-6 activated under vacuum at 200 °C.

929x291mm (300 x 300 DPI)

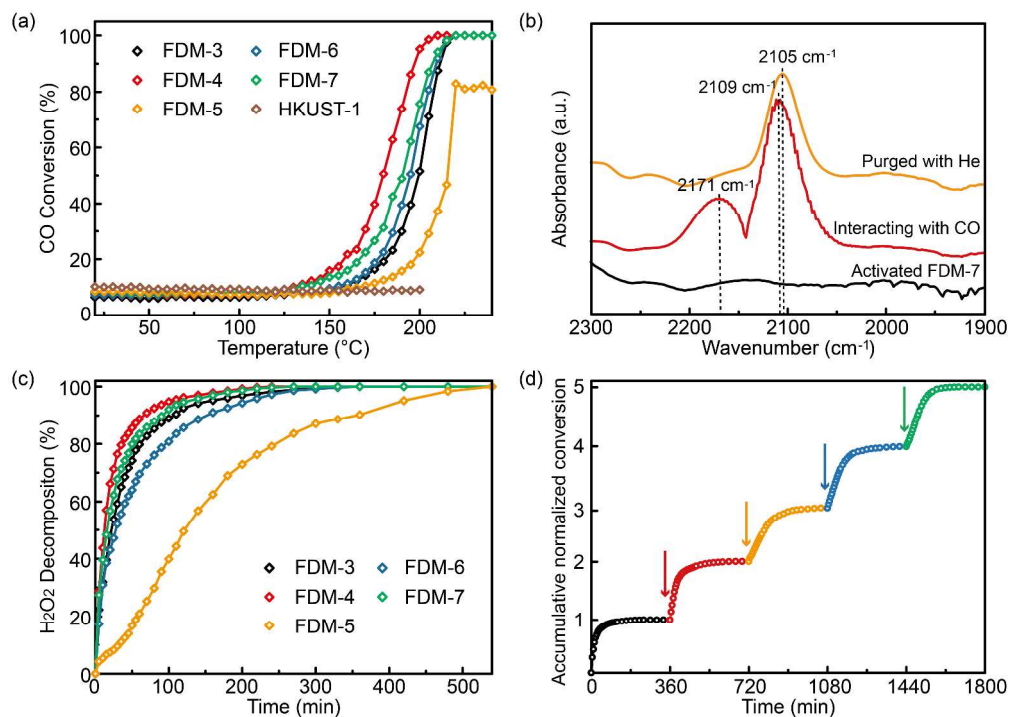
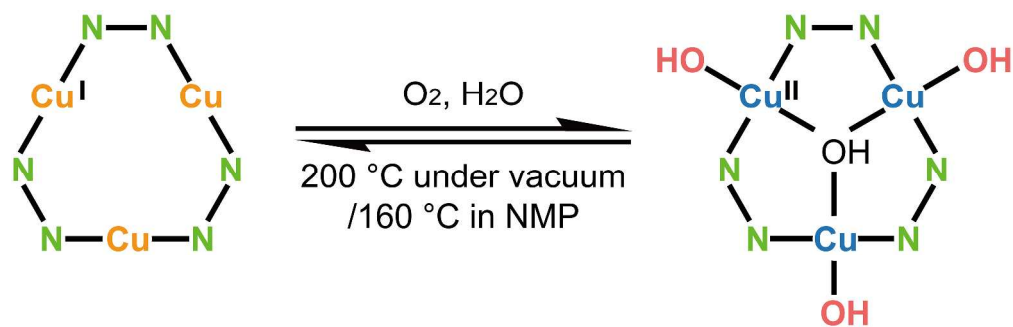


Figure 6. (a) CO conversion as a function of reaction temperature over activated FDM-3–7 and HKUST-1. (b) DFRITS of activated FDM-7 under He flow (black), after interacting with CO (red), and after purged with He (yellow). (c) Results on H₂O₂ decomposition catalyzed by activated FDM-3–7 at room temperature. (d) Performance on five sequential batches of H₂O₂ decomposition over activated FDM-4 at room temperature. The arrows indicate injection of 1 mL H₂O₂ without any regeneration with 6-h interval each time.

427x304mm (300 x 300 DPI)



Scheme 1. The interchangeability of Cu valences in the frameworks of FDM-3-7.

500x163mm (300 x 300 DPI)

